NASA/TM—2017–219680

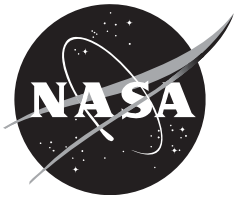

Development of an Axisymmetric Afterbody Test Case for Turbulent Flow Separation Validation

Kevin J. Disotell and Christopher L. Rumsey
Langley Research Center, Hampton, Virginia

November 2017

NASA STI Program ... in Profile

Since its founding, NASA has been dedicated to the advancement of aeronautics and space science. The NASA scientific and technical information (STI) program plays a key part in helping NASA maintain this important role.

The NASA STI program operates under the auspices of the Agency Chief Information Officer. It collects, organizes, provides for archiving, and disseminates NASA's STI. The NASA STI program provides access to the NTRS Registered and its public interface, the NASA Technical Reports Server, thus providing one of the largest collections of aeronautical and space science STI in the world. Results are published in both non-NASA channels and by NASA in the NASA STI Report Series, which includes the following report types:

- TECHNICAL PUBLICATION. Reports of completed research or a major significant phase of research that present the results of NASA Programs and include extensive data or theoretical analysis. Includes compilations of significant scientific and technical data and information deemed to be of continuing reference value. NASA counter-part of peer-reviewed formal professional papers but has less stringent limitations on manuscript length and extent of graphic presentations.

- TECHNICAL MEMORANDUM. Scientific and technical findings that are preliminary or of specialized interest, e.g., quick release reports, working papers, and bibliographies that contain minimal annotation. Does not contain extensive analysis.

- CONTRACTOR REPORT. Scientific and technical findings by NASA-sponsored contractors and grantees.

- CONFERENCE PUBLICATION. Collected papers from scientific and technical conferences, symposia, seminars, or other meetings sponsored or co-sponsored by NASA.

- SPECIAL PUBLICATION. Scientific, technical, or historical information from NASA programs, projects, and missions, often concerned with subjects having substantial public interest.

- TECHNICAL TRANSLATION. English-language translations of foreign scientific and technical material pertinent to NASA's mission.

Specialized services also include organizing and publishing research results, distributing specialized research announcements and feeds, providing information desk and personal search support, and enabling data exchange services.

For more information about the NASA STI program, see the following:

- Access the NASA STI program home page at http://www.sti.nasa.gov

- E-mail your question to help@sti.nasa.gov

- Phone the NASA STI Information Desk at 757-864-9658

- Write to:
  NASA STI Information Desk
  Mail Stop 148
  NASA Langley Research Center
  Hampton, VA 23681-2199

NASA/TM—2017–219680

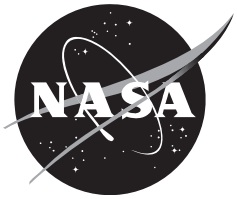

Development of an Axisymmetric Afterbody Test Case for Turbulent Flow Separation Validation

Kevin J. Disotell and Christopher L. Rumsey
Langley Research Center, Hampton, Virginia

National Aeronautics and
Space Administration

Langley Research Center
Hampton, VA 23681

November 2017

Acknowledgments

This research was conducted under the appointment of K.J. Disotell to the NASA Postdoctoral Program at the Langley Research Center, administered by the Universities Space Research Association through a contract with NASA. The support of this appointment by Dr. Mujeeb R. Malik (technical lead, Revolutionary Computational Aerosciences discipline) and the NASA Transformational Tools and Technologies Project within the Transformative Aeronautics Concepts Program are gratefully acknowledged. Feedback from the AIAA Turbulence Model Benchmarking Working Group was valuable in the initial stages of exploration. Prof. Flint Thomas (University of Notre Dame) is thanked for his collaboration on the polynomial ramp contour. Jan-Reneé Carlson, William T. Jones, and Troy E. Lake of the NASA Langley Research Center were instrumental in teaching aspects of FUN3D and grid generation software to K.J. Disotell. Finally, K.J. Disotell acknowledges many helpful discussions with colleagues in the Flow Physics and Control Branch at the NASA Langley Research Center during this work. Final preparations of the manuscript were performed during the faculty appointment of K.J. Disotell at Youngstown State University.

Available from:

NASA STI Support Services
Mail Stop 148
NASA Langley Research Center
Hampton, VA 23681-2199
757-864-9658

National Technical Information Service
5301 Shawnee Rd.
Alexandria, VA 22312
webmail@ntis.gov
703-605-6000

Contents

List of Figures

List of Tables

Abstract

As identified in the CFD Vision 2030 Study commissioned by NASA, validation of advanced RANS models and scale-resolving methods for computing turbulent flows must be supported by improvements in high-quality experiments designed specifically for CFD implementation. A new test platform referred to as the Axisymmetric Afterbody allows for a range of flow behaviors to be studied on interchangeable afterbodies while facilitating access to higher Reynolds number facilities. A priori RANS computations are reported for a risk-reduction configuration to demonstrate critical variation among turbulence model results for a given afterbody, ranging from barely-attached to mild separated flow. The effects of body nose geometry and tunnel-wall boundary condition on the computed afterbody flow are explored to inform the design of an experimental test program.

Symbols

$\langle \bullet \rangle$	=	Ensemble mean value of parameter inside brackets
a	=	Speed of sound
A_S	=	Cross-sectional area of square wind-tunnel test section
C_f	=	Local skin-friction coefficient
C_p	=	Local pressure coefficient
D_M	=	Equivalent tunnel diameter accounting for massflow in square corners
k	=	Kinetic energy of turbulent fluctuations per unit mass
L	=	Axial length of body (no subscript); axial length of body section (subscripted)
M	=	Mach number, ratio of velocity magnitude to speed of sound reference
N	=	Nose-body configuration
NL	=	Noseless-body configuration
p	=	Pressure (context given by subscript)
R	=	Local radius of body
Re	=	Reynolds number based on R_{max}, $Re=U_\infty R_{max}/\nu$
T	=	Temperature (context given by subscript)
u'	=	Fluctuating velocity component in x-direction
u^+	=	Viscous sublayer-scaled streamwise velocity, u/u_τ
u_τ	=	Shear velocity, $\sqrt{\tau_w/\rho_w}$
U	=	Mean flow velocity component in x-direction
w'	=	Fluctuating velocity component in z-direction
x	=	Cartesian coordinate along body axis of revolution
z	=	Cartesian coordinate normal to axis of revolution on $y = 0$ plane
z^+	=	Viscous sublayer-scaled distance normal to wall, zu_τ/ν
ρ	=	Fluid density
δ	=	Local boundary-layer thickness at $0.99U_e$
η	=	Distribution of body radius along axis of revolution, $R(x)$
κ	=	Longitudinal curvature of surface definition
ν	=	Kinematic viscosity of fluid

σ = Ratio of aftbody radius to maximum body radius;
also, standard deviation of parameter Q notated by $\sigma(Q)$

τ_{ij} = Specific Reynolds stress tensor, $-\langle u_i' u_j' \rangle$

ω = Specific dissipation rate

Subscripts

A = Constant-radius aftbody section

B = Boattail section

e = Local value at edge of boundary layer

F = Constant-radius forebody section

max = Global maximum of parameter

N = Nose section

peak = Local maximum of parameter

t = Stagnation conditions

w = Local value at wall

∞ = Value far upstream of body (*i.e.*, test section entrance)

I. Introduction

The CFD Vision 2030 study [1], commissioned by NASA to develop a plan for research investments in simulation-based engineering processes relevant to the aerospace industry, underscored the lack of current reliability in deploying computational fluid dynamics (CFD) to a wide operational design space. In particular, a pervasive issue has been the prediction of viscous flow fields over streamlined bodies with turbulent flow separation present. Besides the inability to accurately predict vehicle drag for arbitrary operating conditions *a priori*, low confidence in edge-of-the-envelope performance predictions can misguide design decisions or defer to overly conservative approaches that sacrifice performance. To further develop, diagnose, and correct advanced physics-based CFD methods for computing turbulent flows, high-fidelity benchmark experiments to be coordinated by NASA were recommended by the CFD Vision 2030 study. In doing so, new validation databases are in the process of being generated for use as community resources to aid modelers; one such effort already underway is the NASA Juncture Flow Experiment [2].

In order to critically assess the accuracy of a computation and its modeling components, the most basic requirement for a validation experiment is a reproducible set of boundary values for the flow physics of interest. Only then can it be assured that a computation is posing the same question of nature as in the "truth" case, which may be a physical experiment or a fully-resolved numerical simulation (*e.g.*, direct numerical simulation). Oberkampf and Roy [3] define validation programs as a unique class of experiment: "…a validation experiment is designed, executed, and analyzed for the purpose of quantitatively determining the ability of the model and its embodiment in a computer code to simulate a well-characterized physical process." For turbulent flows, the difficulty of full characterization is writ large given the range of interacting length and velocity scales in the flow. Thus, the accessibility of measurements also becomes a defining quality of the validation effort. Oberkampf and Roy [3] further describe a hierarchy of validation experiments in terms of physical characteristics and extent of measured data. This hierarchy ranges from unit problems with simple hardware providing isolated physics and the highest level of measurement detail, to complete production systems with full physics but more limited measurement data. All levels contribute insight to design tool validation.

The current work addresses the design and ongoing execution of a new test platform for turbulence modeling validation in wall-bounded flows with separation. A discussion of the philosophy and approach to the test case design is presented. Details on the devised body-of-revolution formulation are then documented, including parameters for a prototype configuration developed for risk-reduction testing. Foundational Reynolds-Averaged Navier Stokes (RANS) computations comprising a sensitivity study on

the effect of *a priori* turbulence model selection on flow behavior for this risk-reduction configuration are presented and discussed. Finally, conclusions drawn from the computational results are summarized to guide a path forward for obtaining a "truth" case requiring experimental and/or direct simulation data.

II. Test Case Development

In this section, the requirements and philosophy underpinning the test case design are documented. The particular focus of the validation effort is described, leading to a discussion of the designed test configuration. Derivation of the body geometry is presented, followed by a description of the integral flow physics relevant to the test case. Finally, industry-relevant applications of the test geometry are highlighted for practical motivation.

Requirements

Of primary interest for turbulence modeling purposes was the ability to produce a range of cases encompassing attached turbulent flow, incipient turbulent separation, and large-scale separation from a smooth surface. Accordingly, a simple mechanism that could be unambiguously duplicated between the experiment and computation was necessary to vary the scale of separation, which amounts to varying the adverse pressure gradient for the desired smooth-body separation. The surface geometry was desired to be relatively simple, such that it could be exactly defined using analytic functions for unambiguous representation by CFD; a two-dimensional or axisymmetric geometry was preferable. This approach was aimed at reducing numerical error due to uncertainty in the geometry definition. Also pertaining to grid considerations, the wind tunnel wall constraints were required to be unambiguously reproduced without undue complexity. The test conditions were to be at sufficiently high freestream Mach number to avoid the use of low-speed CFD preconditioners in compressible flow solvers, which typically suggests $M > 0.1$.

Configuration Decisions

Given the above requirements, early test article concepts turned toward an axisymmetric configuration for several reasons. An axisymmetric body can be mounted more easily than a plane-symmetric model in a larger range of wind tunnel facilities, enabling a wider validation domain in Mach and Reynolds number. In addition, maintaining an accurate surface definition is accomplished more cost-effectively by the turning operation on a lathe compared to the fabrication process required for plane-symmetric models. As an example, Watson *et al*. [4] cited these reasons for the choice of an axisymmetric test model to obtain two-dimensional boundary-layer data in a high-Reynolds-number cryogenic wind tunnel. Axisymmetric bodies-of-revolution with large regions of separated flow have also been tested at high Reynolds number [5], although the data typically consist of pressure coefficient distributions and qualitative surface visualizations rather than detailed flow turbulence measurements. Another advantage of an axisymmetric configuration is avoidance of direct contact between the test model and wind tunnel wall boundary-layers, commonly referred to as "3-D contamination" in plane-symmetric flows aiming for two-dimensional characteristics. This source of three-dimensionality can present ambiguous interference effects for floor-mounted and sidewall-mounted models. Finally, with increasing miniaturization of laser-based measurement systems, a suitably-sized axisymmetric model may also facilitate stowing of measurement equipment in the interior volume of a test body to enable highly-resolved, near-wall turbulence data.

The above advantages motivated an early design decision to pursue an axisymmetric test model. A foundation of experiments exists for axisymmetric geometries in turbulence research, some of which have been recommended as test cases for large-eddy simulation (LES) validation [6]. While not specifically considering flow separation, Winter, Rotta, and Smith [7] studied a waisted body-of-revolution as an analog for a cambered delta wing. The axisymmetric body was deemed to be a more tractable measurement case than the delta wing by avoiding the presence of three-dimensional wing cross-flows, since the streamline convergence/divergence distribution of the delta wing could be made analogous between the two

configurations. The waisted body profile is shown in Figure 1 for reference. The specific effort of Winter, Rotta, and Smith during the 1960s was focused on diagnosing the inability of existing turbulent boundary-layer calculation methods to correctly predict local skin friction in regions of mild adverse pressure gradient combined with streamline convergence near the waist of the body, and considered both subsonic and supersonic attached flow.

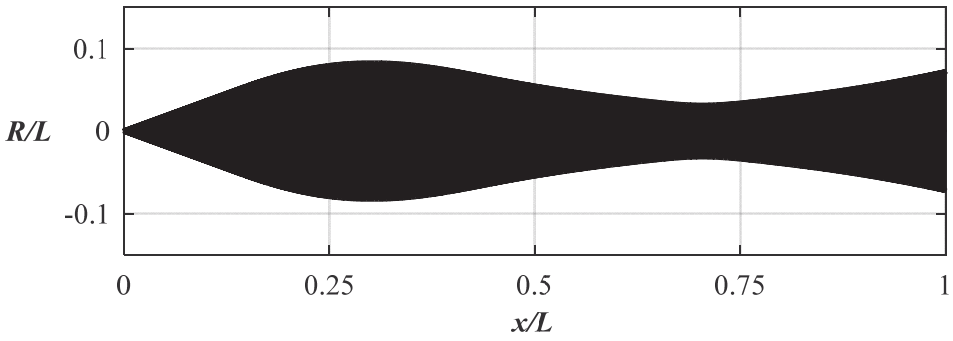

Figure 1. Waisted body-of-revolution profile from Winter, Rotta, and Smith [7].

Particular to turbulent flows with separation, several axisymmetric experiments are noteworthy validation cases. Bachalo and Johnson [8] contributed an advanced validation case in the 1980s for transonic shock/boundary-layer interaction consisting of an axisymmetric bump on a cylinder aligned with the flow direction, in which laser interferometry was deployed for detailed turbulence measurements. Driver [9] reported detailed turbulence measurements in a mild separation bubble produced on a constant-diameter cylinder aligned with the direction of flow in a low-speed wind tunnel (M = 0.088 at inlet). The cylinder occupied the entire streamwise length of the test section and was supported on both ends inside the contraction and diffuser sections of the wind tunnel. The adverse pressure gradient was supplied by diverging all four walls of the initially square test section. This test case included a careful check on axisymmetry of the flow field by quantitative circumferential pressure and skin-friction measurements, as well as a momentum balance using velocity fields measured with a laser Doppler interferometer. Alving and Fernholz [10, 11] conducted detailed hot-wire/pulsed-wire anemometry measurements of turbulent boundary layer relaxation on a smooth, axisymmetric body following a short fetch of mean reversed flow under incompressible conditions.

Certain axisymmetric experiments have made use of interchangeable geometries to study a range of turbulent flow behavior near and beyond separation. Presz and Pitkin [12] as well as Reubush and Putnam [13] studied the compressible subsonic flow over a series of axisymmetric nozzle afterbody models, in which the exhaust plume was approximated by solid blockage in the form of an integrated tail sting. A range of attached, partially-separated and fully-separated flows was obtained by varying the mean angle of the contoured afterbody geometry and different contour shapes. In addition, the incoming turbulent boundary layer properties were parametrically varied by a modular forebody that could be extended in length over a constant-diameter section. Measurements of flow turbulence were not reported in either study. More recently, Hammache, Browand, and Blackwelder [14] provided modern particle image velocimetry (PIV) measurements on an axisymmetric analog to a plane-symmetric Stratford ramp, inversely-derived from a pressure distribution yielding maximum pressure recovery over the shortest streamwise length while barely avoiding separation. Here, the nearly-separated flow exhibits both boundary-layer and wake-like behavior. Two additional ramp shapes with mean angles corresponding to higher and lower adverse pressure gradients were tested for comparison with the zero-skin-friction case. The theme of interchangeable test model stages to vary the scale of separation was appealing for the basis of the current test case design, as an accurate surface definition presents a reproducible boundary condition for CFD.

From the aforementioned studies, it is noted that the body nose was placed in the test section, other than the configuration of Driver [9]. This is both a practical aspect for installation in larger test facilities as well as a physical consideration for boundary-layer development on the test article.

Test Model Geometry

Specification of the test model geometry was guided by several design criteria: (1) minimal surface complexity; (2) a smooth, analytic surface definition to be unambiguously defined; and (3) an ability to parametrically vary the surface contour (and therefore, the flow behavior) through tailoring of the geometry inputs. The choice of an axisymmetric body-of-revolution offers the advantageous property of geometric two-dimensionality, thereby minimizing surface complexity. In determining an appropriate form of the shape-generating equation, it was desired to produce a continuous second derivative of the surface geodesic along the length of the body, as the flow may be sensitive to discontinuities in surface curvature.

To meet the intended requirements, an axisymmetric test body was devised to have four components: (1) an elliptical nose, (2) a constant-radius forebody section, (3) a contoured boattail (ramp) section that is smoothly faired between the fore and aft sections, and (4) a constant-radius aft section. The mean boattail angle is a function of the ratio of the aft-cylinder radius to maximum body radius, σ, as well as the desired axial length of the boattail section. The aft cylinder was desired to be as long as practical for studying relaxation of the perturbed flow over the ramp as well as reducing potential interference effects of the sting strut, which will be characterized during the initial stages of a planned risk-reduction experiment in a wind tunnel. A sample illustration of the parametric, axisymmetric body is shown in Figure 2, with the above sections annotated. The parametric nature of the geometry formulation allows for a series of afterbodies to be investigated in pursuit of a range of flow behaviors. For example, adjustment of the axial length of the constant-radius forebody section can provide different incoming boundary layer conditions ahead of the boattail, and the mean angle of the boattail section can be varied to control the adverse pressure gradient. A representative family of "slip-on" afterbodies is depicted in Figure 3.

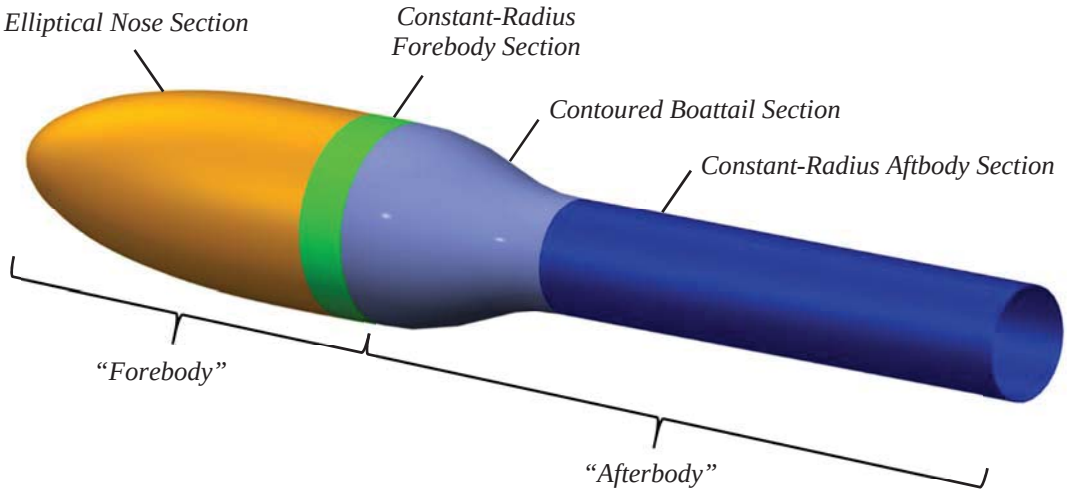

Figure 2. Rendering of isolated test body (σ = 0.575).

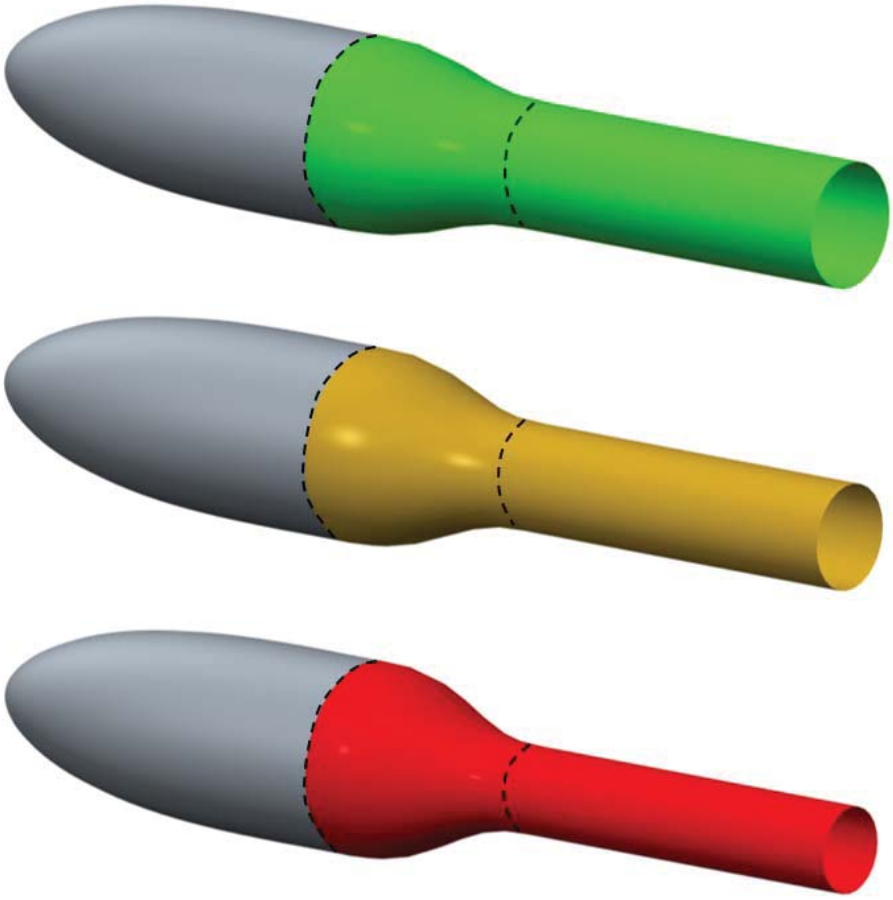

Figure 3. Representative family of afterbodies for achieving range of flow behavior.

In order to satisfy the desire for a continuous second derivative of the surface geodesic, the constant-radius segments posed constraints for the generating equations of the elliptical nose and contoured boattail. The nose shape was selected to be a blended function between an ellipse and fourth-order superellipse, similar to that reported in Watson *et al*. [4] For the boattail, a fifth-order polynomial was selected for its capacity to support three inflection points, two of which are imposed at the end points of the contour to ensure that the first and second derivatives are zero. As formulated, the constructed shape requires a total of six geometric inputs: the maximum body radius, the ratio of aftbody radius to maximum body radius, and axial lengths of the four individual stages previously described. The analytic formulation of this geometry is provided in the Appendix. Throughout this work, the axial origin of the coordinate system, $x = 0$, is taken as the start of the defining equation for the boattail section; in other words, $x < 0$ upstream of the boattail section.

Several of the geometric inputs were strategically selected for a prototype test model under development, which is referred to herein as a risk-reduction configuration. The length of the forebody was dictated by the minimum boundary-layer thickness accessible by measurement (taken to be ~1 cm), which was estimated with CFD calculations. A lower bound on the boundary-layer thickness is necessary for accurate characterization, but the boundary layer was desired to not be so thick relative to the body diameter as to separate with greater severity than is representative of full-scale wings [8]. In addition, selection of the body size was guided by minimization of transverse curvature effects through the condition $\delta/R << 1$, where δ is the boundary layer thickness and R is the local radius of the body, such that the local wall appears "flat" to turbulent eddies. Maximizing the body radius must be balanced by the practical requirement for an

appropriate model scale for test and measurement, as well as avoidance of model sagging due to cantilevered weight. The latter aspect is critical to minimizing three-dimensional flow effects caused by model misalignment.

Turbulence Modeling Aspects

As Smits and Wood [15] stated in their review of perturbed turbulent boundary layers, "The combined influence of different disturbances is rarely given by a simple summation of their separate effects." Additional physical effects may be produced by such interactions among multiple rates of strain, such as surface curvature or lateral divergence, thereby altering the turbulence structure and separation behavior. As new machine-based approaches to turbulence modeling are being explored [16, 17], appropriate training flows embodied in a core of validation experiments (physical or numerical) will be necessary, and by nature can be more conceptually adventurous for exploring complex flows in systematic ways. For the devised parametric body-of-revolution, the fundamental perturbations produced by the afterbody geometry include adverse pressure gradient, lateral streamline convergence, and longitudinal surface curvature (convex and concave, due to the chosen polynomial contour). Smits and Joubert [18] have observed that the combined effect of convergence and convex curvature acts in a stabilizing manner by reducing turbulent mixing, whereas concave curvature by itself is destabilizing. Concave curvature may produce longitudinal roll cells [15] akin to the Taylor-Görtler instability. The nature of curvature effects in particular, including magnitude and response time of flow parameters following the geometry perturbation, has been characterized to be asymmetric depending on whether the curvature is convex or concave [19]. Given these ingredients, the case of attached flow over the boattail is expected to provide useful insight on its own. Modeling issues that can be assessed with this configuration framework are the effect of higher Reynolds number on separation characteristics, meaningful nonequilibrium effects associated with progression from attached to increasingly separated afterbody flows, and the effect of embedded mean flow vortices (*e.g.*, Görtler vortices) on turbulence structure.

Practical Relevance of Configuration

Axisymmetric afterbodies have been studied for decades due to their importance in the aerospace industry. In propulsion applications, nozzle afterbodies (boattails) can be a significant source of parasitic drag with flow separation present. For vehicle configurations with strong engine-airframe coupling, such behavior can strongly influence upstream flow conditions and overall aerodynamic performance. Flow separation at the aft end of aircraft fuselages is also a relevant application area for flow control technology. Finally, a class of space-launch vehicles known as "hammerheads"—with payload diameter larger than the rocket stage below it—have been the subject of buffet testing to quantify unsteady aerodynamic loading effects due to the diameter transition [20], and recent simulations [21] of this configuration have been conducted. While axisymmetric afterbodies have been the focus of many empirical studies, much of the historical data are limited in spatial and/or temporal resolution. For the present work, the above considerations suggested a valuable opportunity to deploy modern experimental techniques to generate state-of-the-art experimental databases for CFD validation purposes on an industry-relevant geometry.

An axisymmetric body also has practical advantages for wind tunnel testing. For example, a typical aircraft model is often heavily instrumented with on-body measurement sensors such as pressure taps and transducers, which must be strategically distributed over the 3-D configuration. Due to the geometric two-dimensionality of a body-of-revolution, instrumentation counts can be reduced when a roll-coupled sting (common in high-priority test facilities) is available to rotate sensors around the circumference of the body to check for flow uniformity, assuming a carefully-manufactured model with negligible coning. With an axisymmetric body, the demands of model deformation measurements (and implementation in CFD) are reduced compared to aircraft models with aeroelastic wing surfaces. Finally, with the ever-increasing miniaturization of measurement hardware, a sufficiently-large axisymmetric body designed for a given test facility could provide a means of stowing instrumentation inside the model—a provision that cannot typically be accommodated by the interior volume of thin wings on aircraft models, for example. This

provision is directly related to higher data quality such as achieved by reducing tubing length to a pressure scanner module, while also opening the possibility for near-wall optical measurements that are crucial to the generation of new flow physics databases. Model-embedded laser Doppler velocimetry (LDV) and particle image velocimetry (PIV) systems are now within the realm of possibility due to increased miniaturization of photodetectors/cameras and laser systems, representing an opportunity to be leveraged for validation-quality measurements.

III. *A Priori* RANS Results and Discussion

Development of the test case was supported by early-stage CFD guidance to demonstrate evidence for critical variations among RANS turbulence models (*e.g.*, barely-attached or mild separated flow) for a given configuration. In this section, details of the numerical setups are presented, followed by results from selected turbulence models for a risk-reduction configuration. Effects of body nose geometry and the wind tunnel boundary-layer are explored. Finally, the effect of outer wall position under the considered approximation of an axisymmetric domain is investigated. The significance of the CFD results are discussed to inform future evolution of the test case.

Computational Setups

Steady RANS computations in fully-turbulent mode were pursued to inform the selection of mean boattail angle for the risk-reduction configuration and assess its potential for serving as a discriminating test case for turbulence models. For this purpose, the flow environment was modeled as a true axisymmetric domain with diameter equal to the side-length of the purely-square, risk-reduction test facility that was identified in early stages of this work. Initial risk-reduction work is planned for the closed-circuit NASA Langley 15-Inch Low-Speed Wind Tunnel, in which the test section is a square cross-section side length of 15.0 inches (38.1 cm). The physical corners of the test section were not considered in the computations at this stage. The flow conditions were $M_\infty = 0.117$ at the test section inlet (corresponding to $U_\infty = 40$ m/s; maximum tunnel speed is near 45 m/s), with Reynolds number based on maximum body radius ($Re = U_\infty R_{max}/\nu$, where ν is kinematic viscosity) of 180,000. The risk-reduction model geometry detailed in the Appendix is exclusively considered herein. As such, the geometric blockage (ratio of maximum cross-sectional area of the body to the cross-sectional area of the test section) was 12.6%; for comparison, the cylinder in parallel flow considered by Driver [9] corresponded to a geometric blockage of 16.6% at the test-section inlet. Structured, axisymmetric grids were created for the intended test conditions using a wedge-shaped domain. The body grid was rotated about the axis of revolution by 1.0 degree, with symmetry boundary conditions imposed on the side planes of the resulting domain. In order to provide a finite width to grid elements upstream of the nose stagnation point, thereby avoiding a line of poles, the axis of revolution was offset below the $z = 0$ axis by a distance of $\Delta z/R_{max} = -0.002$. The finest grid ("F") used a total of 449 points distributed over the body profile in the streamwise direction, with a viscous layer containing 97 points distributed normal to the surface according to a hyperbolic tangent profile (growth factor of 1.05). Flow solutions confirmed the first grid point off the body being below $z^+ = 0.15$ along its entire length for the finest grid. In the radial direction between the edge of the viscous body layer and the tunnel wall boundary, 193 grid points were distributed to represent the outer flow, where the tunnel wall boundary was treated with a viscous layer using 145 points in the wall-normal direction with a hyperbolic tangent distribution (growth factor of 1.05). Figure 4(a) displays the fine grid construction in the vicinity of the body. The grid extended upstream from the nose apex to the physical entrance of the test section located at $x/R_{max} = -22.8$, corresponding to a length of 55.0 inches (21.7 cm), and the outflow boundary was located at the termination of the afterbody ($x/R_{max} = 7.6$). No support structures (*e.g.*, sting support) were included.

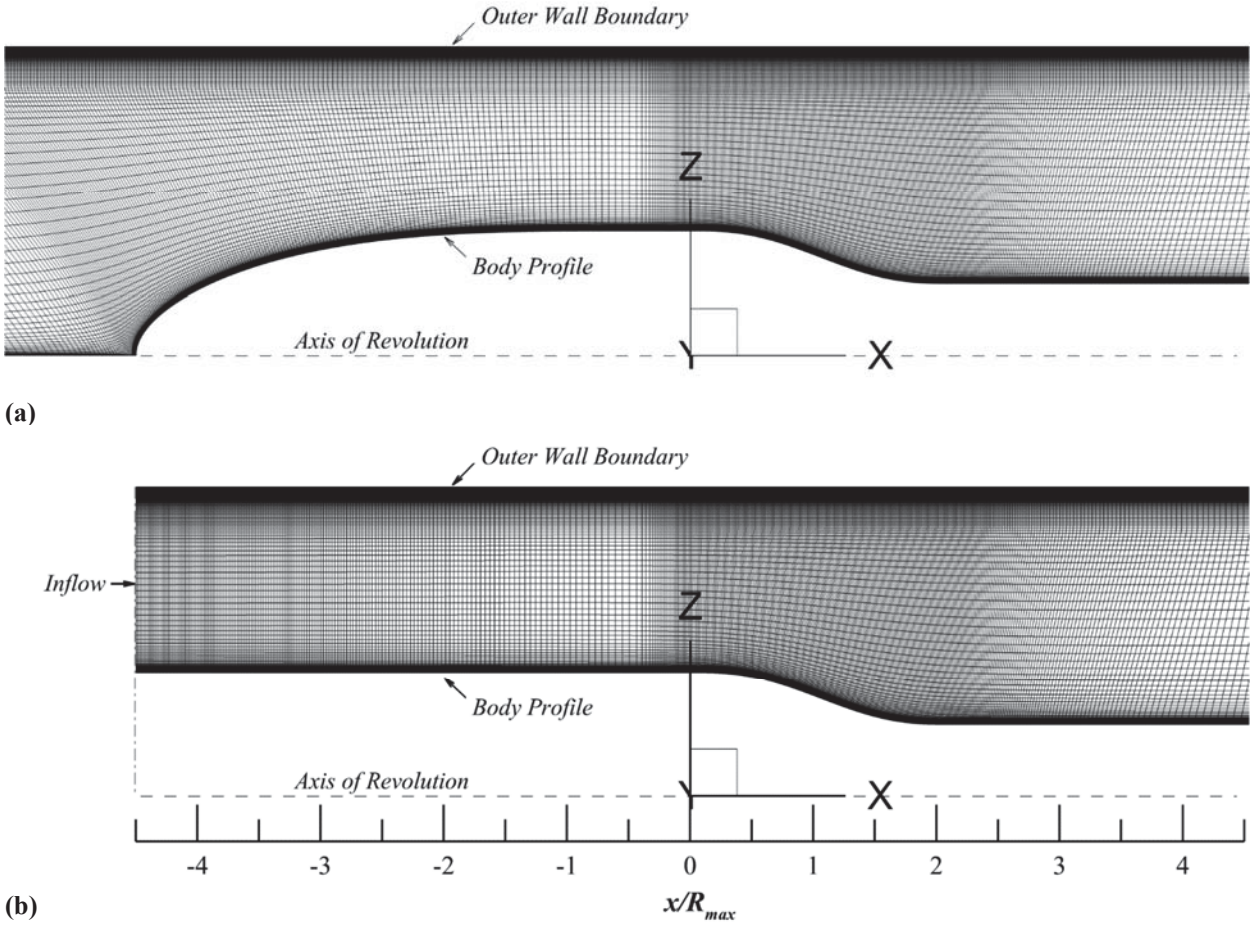

Figure 4. Computational grid (a) in vicinity of nose-body and (b) noseless-body. Flow direction is left to right.

A total of 309,011 points comprised the wedge domain (body and upstream segment of the test section). A subsonic inflow boundary condition was imposed by specifying total pressure ratio ($p_t/p_\infty = 1.00962$) and total temperature ratio ($T_t/T_\infty = 1.00274$), while the outflow condition was specified by setting the static pressure ratio (back pressure $p/p_\infty = 0.998$) such that the desired inflow Mach number of $M = 0.117$ at a point near the entrance to the domain was achieved. In this way, a uniform inflow profile was provided in all cases. The outflow condition required that no reverse flow was present at the exit boundary, which was satisfied in the reported cases. The outer wall boundary was treated with the no-slip condition in all cases other than when studying the explicit effect of the tunnel wall boundary-layer on the afterbody flow, in which case the outer wall boundary was treated with an inviscid tangency condition.

In order to study the effect of nose geometry on the afterbody flow behavior, the limiting case of a "noseless body" concept was pursued. The elliptical nose section of the body was replaced by a constant-radius segment having identical axial length and grid point distribution as the elliptical nose, essentially representing an upstream-extension of the constant-radius forebody section. The fine grid construction for the noseless body is shown in Figure 4(b). This concept required the inflow plane to be located at the start of the constant-radius segment replacing the nose, while the outflow plane remained the same as for the nose-body. The axis of revolution was taken as $z = 0$ for the noseless body in order to create a wedge-type domain using the same boundary condition setup as for the nose-body. With the truncated entrance length, a total of 259,522 points comprised the noseless domain.

Grid Resolution and Solver Comparison Study

An assessment of grid resolution was conducted by considering the results from a single turbulence model (SA-RC) using a coarsening factor of two between successive grid levels. Two coarsening levels below the fine grid were primarily considered, identified as medium (*M*) and coarse (*C*). In addition, the resulting grid family was input to two CFD solvers in order to assess code-to-code differences. The two solvers considered were CFL3D [22] (V6.7) and FUN3D [23] (V12.9), both developed at NASA. The grid convergence and code-to-code comparisons were cast using skin-friction coefficient C_f along the boattail length for the nose-body. These results are shown in Figure 5, with the associated boattail region depicted at the top. (For clarity, the exact radial positions of the body contour have been omitted in this type of layout; the exact values of $R(x)$ corresponding to the labeled abscissas may be calculated directly from the analytic function for the boattail as detailed in the Appendix.) The difference between grids *M* and *C* is larger than the difference between grids *M* and *F*, with the results from grid *F* essentially overlaying those of grid *M*. Taken together for both codes and finer grid levels considered, extremely small differences in C_f appear in the region of flow relaxation toward the end of the boattail. An extra-coarse (*XC*) grid computed by CFL3D is shown for reference to further demonstrate the effect of coarsening, in which the C_f value does not approach zero as closely as the finer grids. Having demonstrated the level of agreement for the two considered codes, FUN3D was used for the remainder of the reported results.

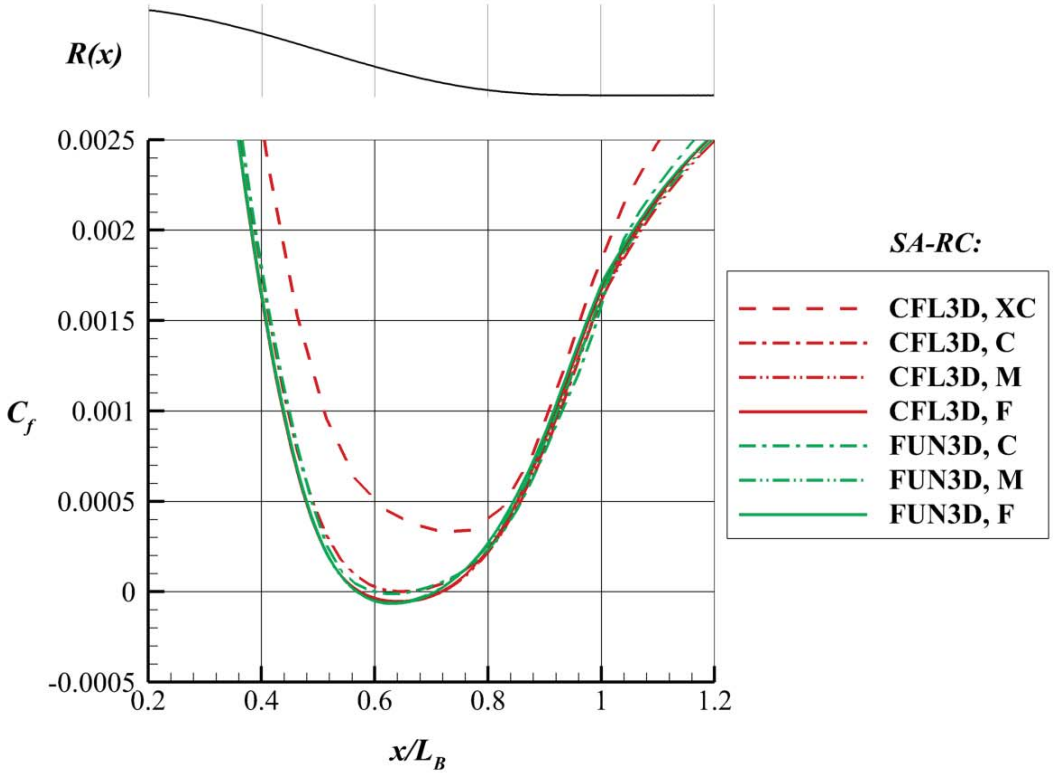

Figure 5. Grid resolution and code comparison results for C_f over boattail region (SA-RC model).

Convergence of Solutions

The solution obtained using each of the turbulence models presented in this work was fully converged by continuing to iterate until the L2-residual computed across the domain reached a steady state. In doing so, deep convergence approaching machine-zero was obtained; in each case, the residuals were reduced to at least 15 orders of magnitude. A representative convergence history is shown in Figure 6 for the SST

turbulence model. The wall time required to reach the total number of iterations shown (approximately 806,000) on the NASA Langley mid-range cluster using 60 processing cores was 100 hours. A sample convergence history for a seven-equation, full Reynolds stress model (WilcoxRSM-w2006), is shown in Figure 7, demonstrating the similar level of deep convergence attained (at least 15 orders of magnitude decrease in residual) despite the larger number of equations solved for the turbulence model.

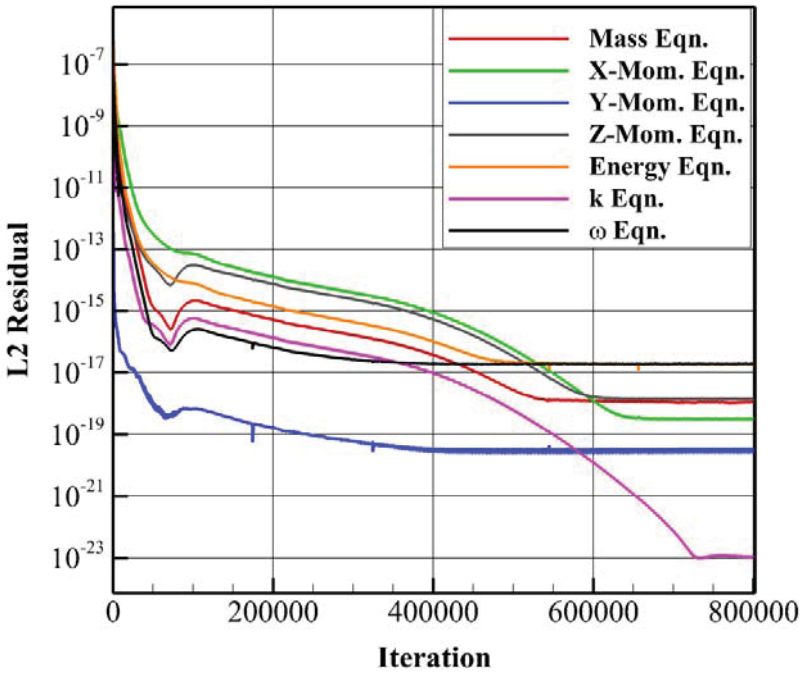

Figure 6. Residual convergence history with SST turbulence model (nose-body).

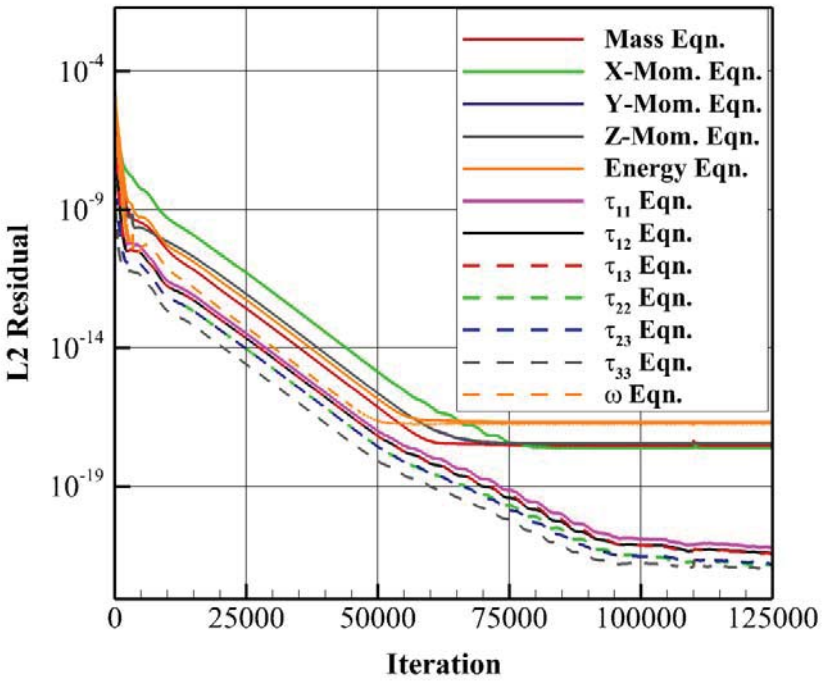

Figure 7. Residual convergence history with WilcoxRSM-w2006 turbulence model (noseless-body).

Representative Flowfields

To provide a basis for results described in the remainder of this section, representative flowfields for the risk-reduction configuration as well as the conceptual noseless-body were computed using the SA-RC turbulence model, and are shown in Figure 8. Both on-body and off-body flows are plotted, cast in terms of skin-friction coefficient and streamwise Mach number (U/a_∞) contours, respectively. Streamlines are also plotted for the off-body flow.

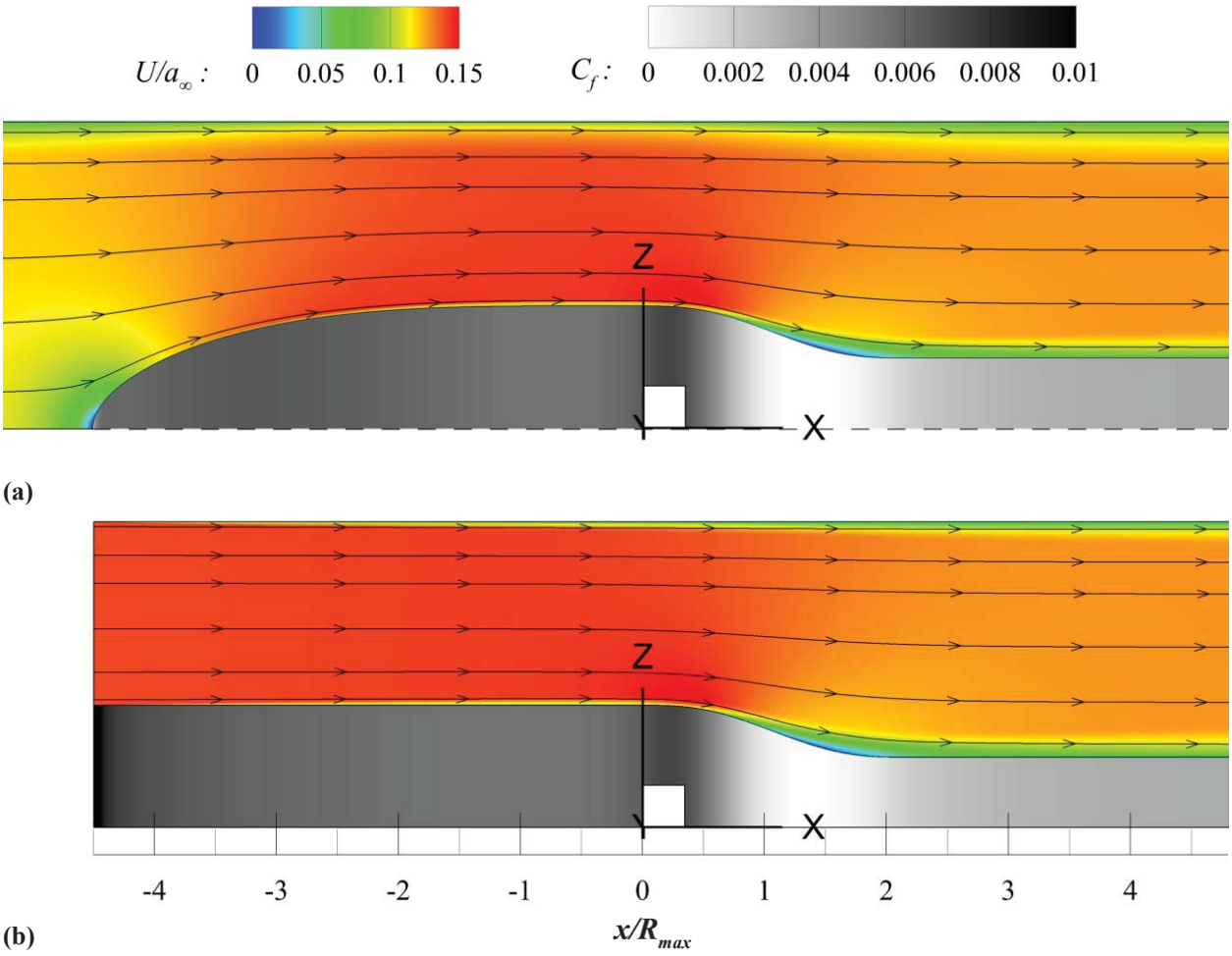

Figure 8. On/off-body flows using SA-RC turbulence model: (a) nose-body; (b) noseless-body.

For the nose-body, the flow accelerates around the nose region until the solid blockage of the forebody section becomes approximately constant. At a distance of R_{max} upstream of the start of the boattail section (*i.e.*, x/R_{max} = -1.0), the boundary layer thickness was determined to be δ = 0.13 inch (3.4 mm), corresponding to a local δ/R = 0.045. For the noseless body, the same station yielded a larger δ = 0.19 inch (4.8 mm); this difference compared to the nose case is attributed to the thinning effect of the favorable pressure gradient associated with the rounded nose. The location of numerical transition, near which the turbulent eddy viscosity begins to exceed the molecular viscosity, was found to occur at approximately 1.0 inch (2.54 cm) downstream of the nose tip in each of the turbulence models for the nose-body.

Near the start of the boattail ($x = 0$), the flow accelerates due to the local convex curvature as C_f increases. The flow then decelerates over the boattail in the presence of concave curvature while accommodating the increasing pressure gradient, as C_f drops to near zero—indicating flow on the verge of separation. The calculated flow over the outer boundary wall does not indicate separation. After the boattail, the relaxing flow carries a larger momentum deficit while C_f increases downstream. The local boundary-layer thickness is approximately $\delta = 0.59$ in. (15.0 mm) for the nose-body at $x/R_{max} = 4.0$, corresponding to $\delta/R = 0.34$. Qualitatively, it is observed that the flowfield solutions for both body configurations are structurally similar beyond $x/R_{max} \sim -1$.

Turbulence Model Comparison: Effect of Nose

An ensemble of turbulence models implemented in FUN3D was studied to assess variability in the flow solutions. Seven turbulence models were considered, ranging in complexity from one-equation models to full Reynolds stress models (RSMs). The ensemble of models included the Spalart-Allmaras model ("negative" version, SA-neg), SA-neg with rotation/curvature correction (SA-RC), Menter's standard SST two-equation model (SST), Wilcox's two-equation k-ω model (Wilcox2006), the k-kL model from Menter/Egorov and Abdol-Hamid (k-kL-MEAH2015), as well as the seven-equation, omega-based Reynolds stress models consisting of Wilcox's RSM (WilcoxRSM-w2006) and the SSG/LRR-RSM-w2012 model. For complete formulation details, the reader is referred to the compendium of models at the NASA Langley Turbulence Modeling Resource*. (The above model abbreviations follow the convention of the NASA Langley Turbulence Modeling Resource.) In each case, no "tuning" of model parameters was conducted; the default model parameters as implemented in FUN3D V12.9 were accepted.

As implemented in FUN3D V12.9, the RSM cases required the symmetry planes of the numerical domain to be aligned with Cartesian axes. This required the two RSM cases to be computed on quarter-plane symmetric domains rather than the wedge domains described previously. For this purpose, the wedge domain was rotated about the axis of revolution with azimuthal step increments of 5.0° to encompass a total angle of 90° for the RSM cases. Due to the increased number of grid points and available computing resources at the time of this work, the RSM cases were only calculated for the noseless-body concept.

For compactness, the solution associated with each turbulence model considered is presented for the nose-body and noseless-body in the following discussion. Figure 9 presents the results cast in terms of pressure coefficient along the body beginning at R_{max} upstream of the boattail section, with the body geometry associated with the given axial limits plotted at the top. The solution in each case was fully converged, with residual levels at 10^{-15} or less (including the RSM cases). Cases with the noseless-body are denoted by the dashed line, while a solid line of the same color represents the accompanying nose-body result using the specified turbulence model. The flow conditions between the nose-/noseless-body cases at $x/R_{max} = -1.0$ differ as expected, yet all the models and nose cases show qualitative agreement as the flow accelerates near the start of the boattail ($x/R_{max} = 0$). Taking together all the cases shown, the standard deviation of peak C_p near the boattail start is within 1% of the average result (0.93%), affirming that the different flow solutions are in close agreement at this station on the body.

---

*URL: http://turbmodels.larc.nasa.gov

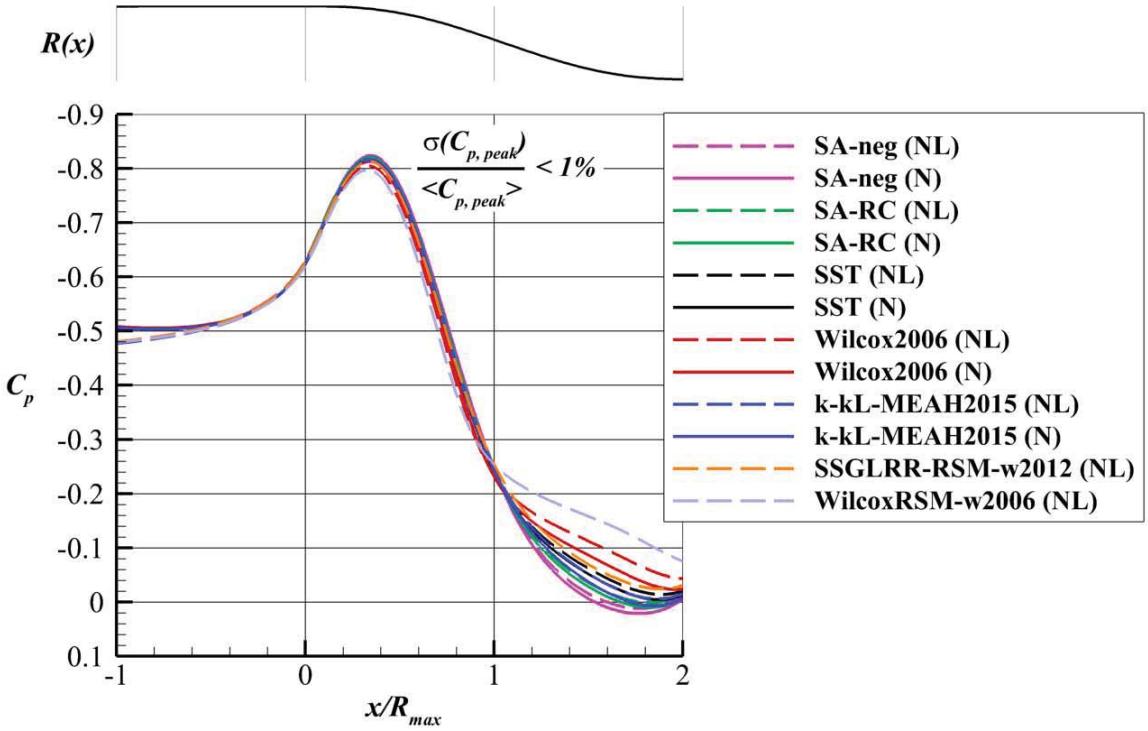

Figure 9. Pressure coefficient distribution in vicinity of boattail section.
Results shown for nose-body (N) and noseless-body (NL) using range of turbulence models.

Boundary-layer profiles at an effective inflow station on the nose-body of $x/R_{max} = -0.5$ (upstream of the boattail start at $x = 0$) are plotted for reference in Figure 10 (inner-layer scaling) and Figure 11 (outer-layer scaling) for several different turbulence models (SA-RC, SST, Wilcox2006, k-kL-MEAH2015). Line symbols are used to convey the grid resolution of the extracted boundary-layer profile; approximately 100 points were captured within the boundary-layer at the given station. The degree of profile variation, particularly in the overlap region between the inner/outer portions of the boundary-layer structure, among the indicated turbulence models is of the same magnitude as that observed in the pressure and skin-friction coefficients. Inspection of the skin-friction distribution in this region, shown in Figure 12, indicates a larger variance in peak C_f compared to the level of agreement in C_p, yet still within 3.5% of the ensemble mean. It is to be noted that the length of the forebody for the noseless-body concept was not tuned beyond matching the axial length of the nose-body; therefore, better agreement could be obtained by iterating on the appropriate length for the constant-radius forebody section. Following the region of acceleration, the flow over the afterbody decelerates under an adverse pressure gradient, in addition to the effect of streamline convergence present with decreasing body diameter. In this region, the effect of the body nose for a given turbulence model is within the variation observed in peak C_p. However, the variation between turbulence models is much larger in the adverse pressure-gradient region. This type of behavior in achieving close agreement at an effective inflow plane followed by divergence among turbulence model solutions downstream is the basic goal of the present validation test case design.

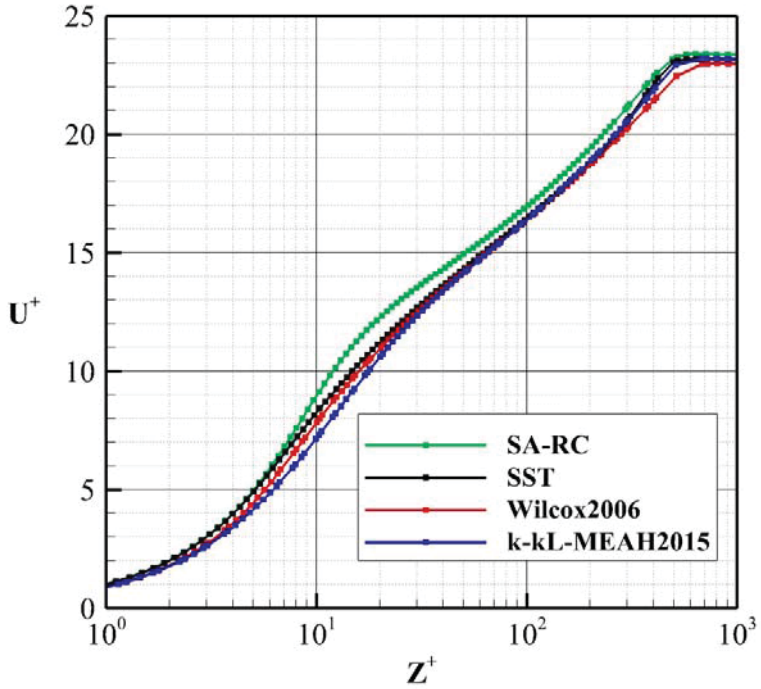

Figure 10. Boundary-layer profiles from turbulence models at x/R_{max} = -0.5 (inner scaling; nose-body).

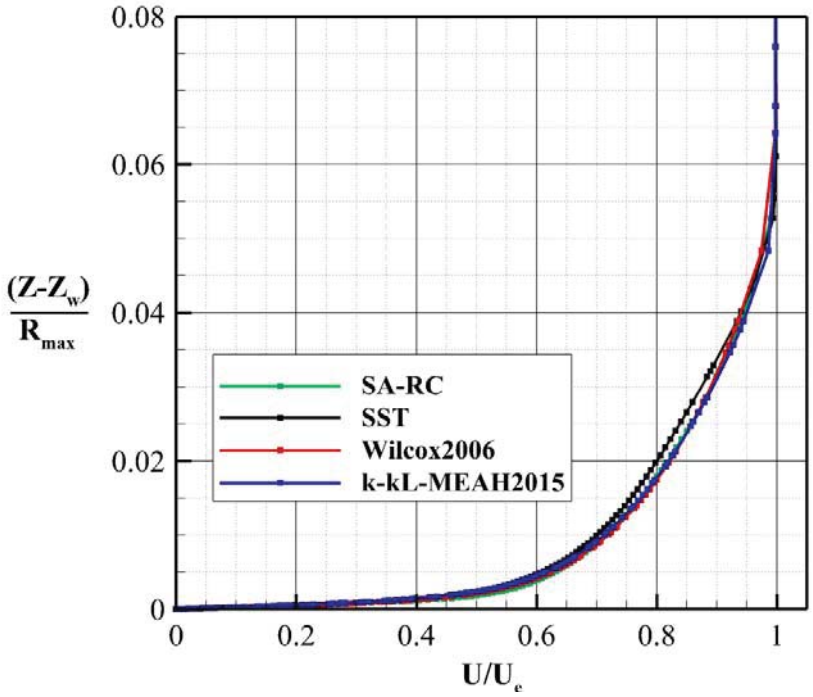

Figure 11. Boundary-layer profiles from turbulence models at x/R_{max} = -0.5 (outer scaling; nose-body).

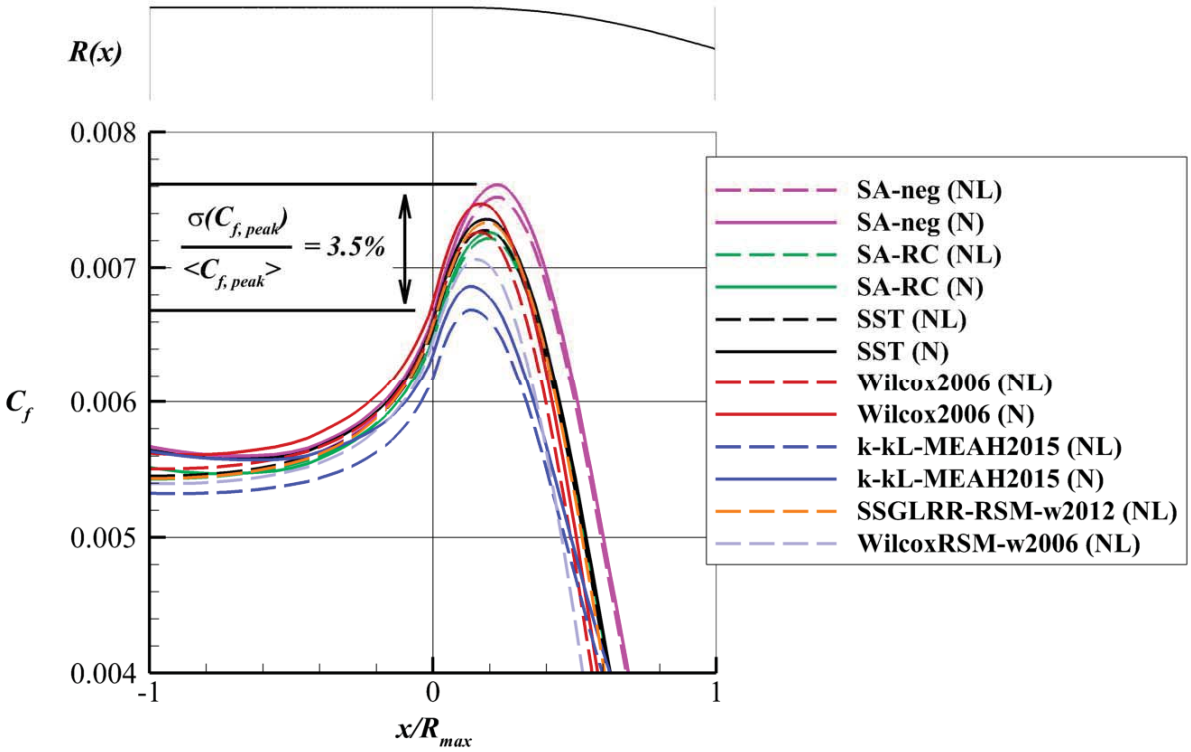

Figure 12. Skin-friction distribution near initiation of boattail section.
Results for nose-body (N) and noseless-body (NL) using range of turbulence models.

Focusing on the afterbody flow, the skin-friction distribution is shown in Figure 13. Without devoting detailed attention to model form differences, two aspects of the data are noteworthy. First, critical differences in near-separation behavior are shown for the range of turbulence models tested. On the basis of C_f, these behaviors range from attached flow to small separated flow, with several models (SA-RC, SST, and SSGLRR-RSM-w2012) on the verge of separation showing fine differences in the existence of reversed flow as indicated by $C_f < 0$. The result from the k-kL-MEAH2015 model is closer to the base SA model without rotation/curvature correction, farther above $C_f = 0$ than the other models considered. Second, the effect of the nose for a given turbulence model is smaller than the overall range of difference among turbulence models. The largest differences due to nose geometry are observed in the relaxation region where C_f begins to increase again, although the k-kL-MEAH2015 model shows the largest difference in nose effect near its local minimum in C_f ($x/L_B \sim 0.65$).

The Wilcox k-ω model as well as the omega-based RSM (WilcoxRSM-w2006) both indicate mild separation. For the nose-body case, SA-RC indicates barely-reversed flow, while SST barely fails to indicate reversed flow. The SA-neg model (without rotation/curvature) and k-kL-MEAH2015 models—which bracket the maximum and minimum limits of peak C_f variation shown previously in Figure 12, respectively—both indicate attached flow. The other RSM studied (SSGLRR-RSM-w2012) for the noseless-body case indicates flow momentarily on the verge of reversal prior to relaxation. Streamwise velocity profiles extracted from the nose-body configuration at $x/L_B = 0.60$ for a subset of turbulence models are shown in Figure 14, highlighting fine differences in flow structure nearest to the wall. The velocity profiles complement the skin-friction distribution shown in Figure 13, with the velocity gradient at the wall near zero for the SA-RC and SST models. Symbols are included on the line plots to convey the level of grid resolution in the extracted flow profiles.

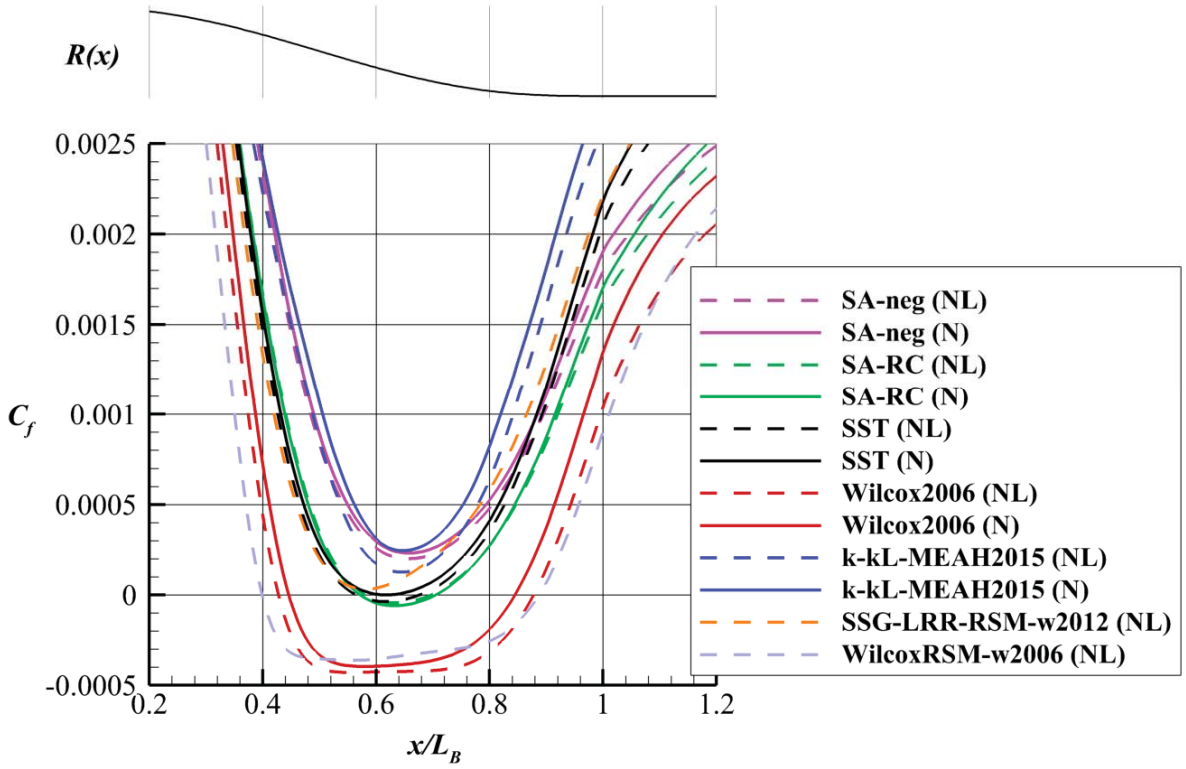

Figure 13. Skin-friction distribution on afterbody.
Results for nose-body (N) and noseless-body (NL) using range of turbulence models.

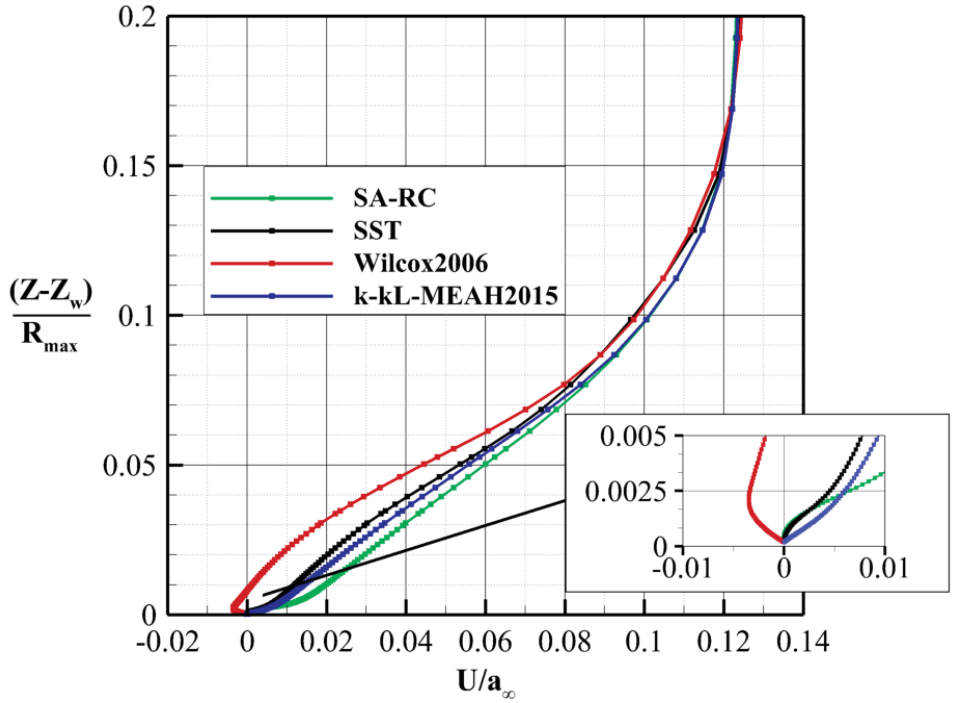

Figure 14. Mean streamwise velocity profiles at x/L_B = 0.60 for set of turbulence models (nose-body).

The above ambiguity in afterbody flow behavior suggests that the boattail geometry is an excellent candidate for challenging the models. A "truth case" in the form of experimental measurements or direct numerical simulation (DNS) is needed to assess the accuracy of the models. Inspection of the computed Reynolds shear stress profiles at station $x/L_B = 0.625$ indicated that the peak value of $-\langle u'w' \rangle$ was located near a height of 4.0 mm above the wall; this site should be accessible with laser-based measurement methods, such as particle image velocimetry. Finally, the fact that the nose geometry (*i.e.*, N or NL) did not fundamentally change the ambiguity in flow behavior on the boattail should be encouraging for implementation in higher-fidelity simulations such as DNS and large-eddy simulation (LES). With generation of turbulence at the inflow plane being a nontrivial task [24], the noseless-body may facilitate implementation of such schemes compared to a stagnation-point calculation for the nose-body. For the goal of model validation, conceptual geometries based on the noseless-body could prove to be fruitful for building databases that encompass the strain effects at play for the afterbody.

Turbulence Model Comparison: Effect of Tunnel Wall Boundary Layer

Given the compact flow domain and relatively large model-to-tunnel-size ratio for the risk-reduction configuration, a study focused on the impact of the wind tunnel wall boundary-layer on afterbody flow behavior was conducted. Here, the term "wind tunnel wall" is used loosely, as the numerical domain is in fact an axisymmetric approximation to the physically square test-section geometry; in addition, the boundary layer thickness does not identically match the physical configuration, as the wind tunnel contraction/upstream leg was not included in the domain. For the purpose of study, the same grid for the nose-body was utilized while only changing the outer wall boundary condition from no-slip to slip. In nearly all cases with outer-wall slip, the flow solution was fully converged with residual levels at 10^{-15} or less. This property was not satisfied for the SA-RC case with outer-wall slip, as the residuals failed to asymptote or diminish below 10^{-9}. The convergence difficulty was traced to the numerical transition zone near the nose apex, where turbulent eddy viscosity is on the order of the molecular eddy viscosity. However, the flow over the remainder of the body was well-behaved and deemed to be suitable for inclusion with the results.

Results comparing outer-wall boundary conditions (slip/no-slip) for the nose-body are plotted in Figure 15. Results for the slip tunnel wall are shown as dashed lines, while a solid line of the same color for a given turbulence model denotes the viscous tunnel wall case. It is evidenced that the effect of the tunnel wall boundary layer for a given turbulence model is smaller than the overall range of difference among models. Comparison with the results shown previously in Figure 13 suggests that the effect of the outer-wall boundary layer alone is smaller than the combined effect of the nose geometry and truncated entrance domain in the noseless-body case. (Recall that the noseless-body results in Figure 13 also incorporate a thinner outer-wall boundary layer due to the truncated entrance domain.) This suggests that reduced computational expense through inviscid treatment of the outer wall is possible without fundamentally altering the variation among turbulence model results for this case.

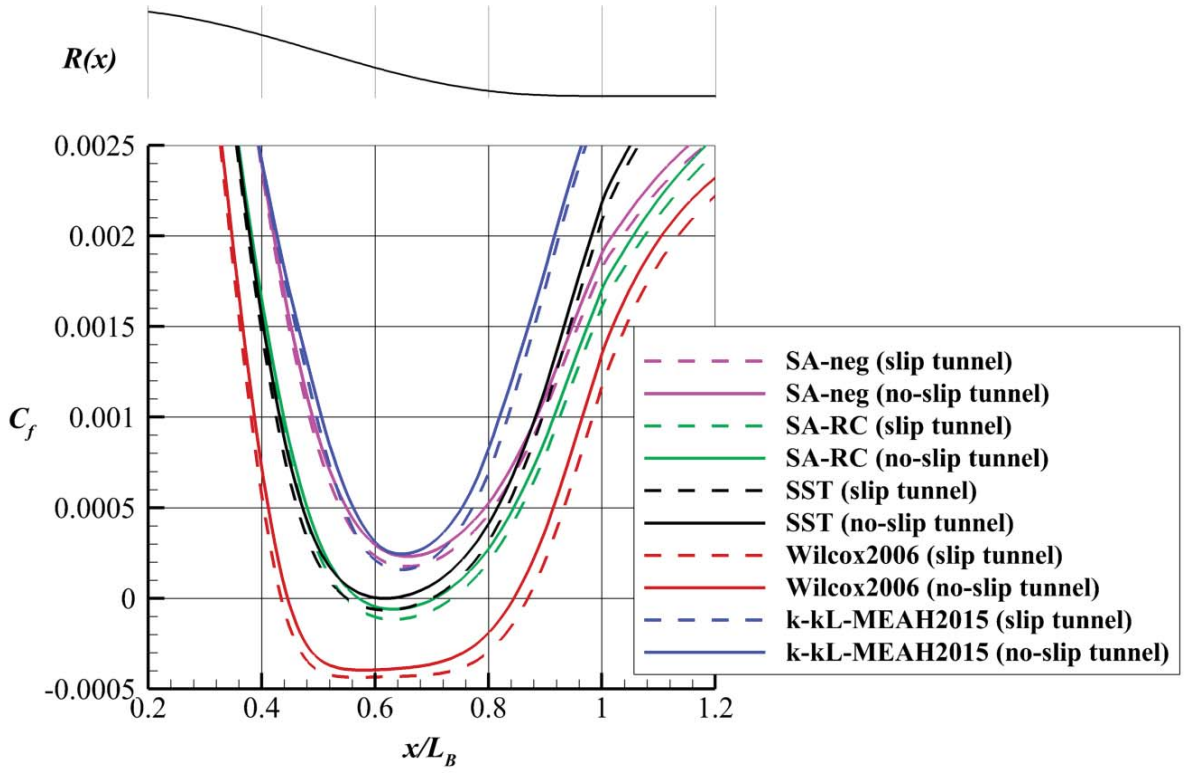

Figure 15. Boattail skin-friction distribution with outer-wall slip/no-slip conditions (nose-body).

Turbulence Model Comparison: Effect of Tunnel Wall Position

A parametric study was also conducted using the noseless-body concept to investigate the influence of the outer wall position. The wall was moved outward to correspond to the diameter necessary to match the massflow of the physically-square test-section, in order to account for the massflow in the square corners that is neglected in the simplified axisymmetric domain based on the inscribed diameter of the physical test section used heretofore. The massflow-matched diameter (D_M) was determined according to Equation (1):

$$D_M = \sqrt{\frac{4A_S}{\pi}} \tag{1}$$

where A_S is the cross-sectional area of the square test section. For the 15-inch wind tunnel, the necessary increase in equivalent radius for the computational domain relative to the inscribed-diameter approach (i.e., diameter equal to side-length of the square cross-section) was 12.8%. The grid for the inscribed-diameter domain was modified to accommodate the change in outer-wall position, with the spacing of grid points in the radial direction in the effectively inviscid region between the body and tunnel-wall boundary layers being retained while "enriching" the grid. Twenty-two grid lines were added to this region to accommodate the increase in outer-wall position (8.25% increase in total number of cells). The results shown in Figure 16 indicate that there is a small influence of the outer wall change on the afterbody flow, with the increase in wall distance providing an expected relieving effect on the adverse pressure gradient. Accordingly, the skin-friction over the boattail increases for the massflow-matched cases. However, the results still indicate that the devised axisymmetric shape is appropriate for discriminating between turbulence models.

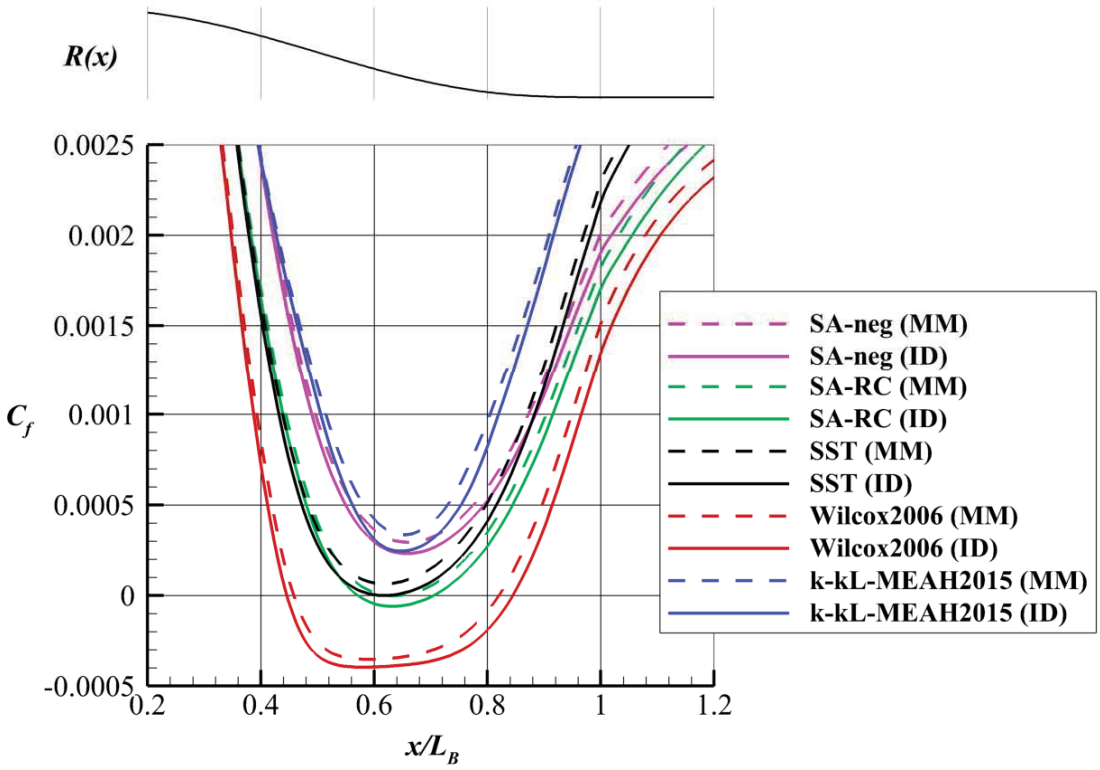

Figure 16. Boattail skin-friction distribution for massflow-matched (MM) and inscribed-diameter (ID) outer-wall positions relative to physical wind tunnel with set of turbulence models (noseless-body).

IV. Conclusions and Future Work

The development of a new CFD validation platform based on a parametric body-of-revolution, referred to as the NASA Axisymmetric Afterbody, was presented in this work. A six-parameter body with continuous second derivative of the surface definition was detailed for studying a range of smooth-body turbulent flow cases, varying from attached to separated boundary-layer behavior. The afterbody flow includes combined effects of curvature, adverse pressure gradient, and streamline convergence having practical importance in aerospace industry applications. Critical ambiguity in computed flow behavior for a selected risk-reduction configuration was documented using a range of RANS turbulence models implemented in FUN3D. Turbulence model results ranged from barely-attached to mild separated flow for the described configuration. Exploration of nose effects as well as the tunnel boundary-layer on afterbody flow behavior demonstrated that fundamental differences between turbulence models were larger than either of these factors. For the considered approximation to the planned risk-reduction configuration using an axisymmetric computational domain, the outer wall position defined by either the inscribed diameter or massflow-matched diameter corresponding to the physically square test section was shown to yield similar ambiguity in afterbody flow behavior.

Taken together, the results reported herein demonstrate that the studied afterbody configuration can serve as a discriminating test case for turbulence models aimed at improving near-and-beyond separation behavior. A “truth case” must now be pursued to assess the *a priori* turbulence model results. Based on the RANS computations described in this work, it was evidenced that the test case can be suitably adapted for either an experimental test campaign using the nose-body configuration, or conceptualized for scale-resolving simulations (LES/DNS) using the noseless-body. The parametric body-of-revolution can also serve as a multirole platform by virtue of its interchangeable afterbody, which may be facilitated by “slip-

on" component configurations in wind tunnel testing. This configuration advantage, as well as the opportunity to integrate stowed instrumentation inside a sufficiently-large test body for a given facility, appeals to the need for high-quality databases as the next-generation core of validation experiments are considered. Such a platform would allow higher Reynolds number testing across a parametric space to generate an encompassing CFD validation database for turbulence modelers.

Appendix: Body Geometry Formulation

This appendix provides details for the parametric surface definition of the body herein referred to as the NASA Axisymmetric Afterbody, a shape derived from analytic functions. Following the parametric formulation, details for the initial risk-reduction model geometry are documented.

Parametric Geometry Definition

Four sections comprise the isolated body (*i.e.*, no model support hardware): (1) elliptical nose, (2) constant-radius forebody extension, (3) contoured boattail, and (4) constant-radius aftbody. The entire body is specified by six parameters: the maximum body radius (R_{max}), the ratio of aftbody radius to maximum body radius (σ), and the axial length (L) of the four individual stages. In each definition, the coordinate system assumed below is such that x is the coordinate along the axis of revolution increasing in the direction of the mean flow, and R is the radial coordinate normal to x. The axial origin of the coordinate system, $x = 0$, is taken as the start of the defining equation for the boattail section; in other words, $x < 0$ upstream of the boattail section.

Elliptical Nose Section

The nose section is designed to smoothly engage the flow near the stagnation point. The nose shape is generated from a standard ellipse blended with a fourth-order super ellipse, similar to that used by Watson *et al.* [4] in which a third-order super ellipse was blended with a standard ellipse. A fourth-order super ellipse was chosen to reduce the bluntness (in reference to axial distribution of cross-sectional area) of the nose while approaching zero curvature at the cross-over between body segments. The nose definition is given by Equation (2a) as:

$$R(x) = r_1\left(1 - \frac{x + L_F + L_N}{L_N}\right) + r_2\left(\frac{x + L_F + L_N}{L_N}\right) \;;\; -(L_F + L_N) \le x \le -L_F \tag{2a}$$

with

$$r_1 = R_{\max}\left[1 - \left(\frac{x + L_F}{L_N}\right)^2\right]^{1/2} \tag{2b}$$

$$r_2 = R_{\max}\left[1 - \left(\frac{x + L_F}{L_N}\right)^4\right]^{1/4} \tag{2c}$$

where R_{max} is the specified maximum body radius, L_N is the axial length of the nose section, and L_F is the axial length of the constant-radius forebody section.

Constant-Radius Forebody Section

The constant-radius forebody section provides a convenient experimental control for incoming boundary-layer properties to the afterbody. It may be extended or shortened to allow for a desired boundary-layer thickness, for example. The right-cylindrical section is expressed by Equation (3) as:

$$R(x) = R_{\max} \;;\; -L_F \le x \le 0 \tag{3}$$

Contoured Boattail Section

For the boattail, a fifth-order polynomial was selected for its capacity to support three inflection points, two of which are imposed at the end points of the contour to ensure that the first and second derivatives are zero. The boattail section is expressed by Equation (4a) as:

$$R(x) = a_1 + a_2 x^3 + a_3 x^4 + a_4 x^5 ;\ 0 \le x \le L_B \tag{4a}$$

with

$$a_1 = R_{\max} \tag{4b}$$

$$a_2 = \frac{-10 R_{\max} (1-\sigma)}{L_B{}^3} \tag{4c}$$

$$a_3 = \frac{15 R_{\max} (1-\sigma)}{L_B{}^4} \tag{4d}$$

$$a_4 = \frac{-6 R_{\max} (1-\sigma)}{L_B{}^5} \tag{4e}$$

where σ is the ratio of the minimum aftbody radius to the maximum body radius and L_B is the axial length of the boattail section.

Constant-Radius Aftbody Section

The axial length of the constant-diameter aftbody section is intended to be adjustable as needed in order to provide a sufficient relaxation distance for the flow after encountering the boattail section, since measurements of the flow recovery can be of interest. Furthermore, the aftbody length has a practical consideration in providing sufficient separation from the downstream test model support system. The right-cylindrical aftbody section is expressed by Equation (5) as:

$$R(x) = \sigma R_{\max} ;\ L_B \le x \le \left(L_B + L_A\right) \tag{5}$$

From the perspective of wind tunnel testing, a minimum length L_A can be suggested by consideration of model support interference effects. With many studies of sting/support interference having been reported in the literature for various sting-mounted bodies, the constant-radius aftbody section attempts to mitigate the influence of the sting by close integration of component diameters, thereby minimizing exposure of a significant base region. An aftbody length L_A of at least 5 model base-diameters, where the base diameter referred to here is expressed as $2\sigma R_{\max}$, is near the lower limit from the interference study of Tunnell [25]. Typical sting mounts may also have a flare, a tapered insert to the model base, which precedes the sting shaft to augment structural integrity at the model connection. Here, the sting flare diameter should not exceed the aftbody diameter in order to minimize upstream influence, and struts supporting the sting should minimize frontal blockage.

Risk-Reduction Test Model

A prototype test model to be built for risk-reduction experiments was guided by CFD calculations that alluded to key variations in flow behavior using different turbulence models. Table 1 lists the parameter set for the risk-reduction body.

Table 1: Parameter set for risk-reduction body.

Parameter	Value
R_{max}	3.0 in.
L_N	$4.0R_{max}$
L_F	$0.5R_{max}$
L_B	$2.1R_{max}$
L_A	$5.5R_{max}$
σ	0.575

The divergence and curvature parameters of the geometry—being proportional to the first and second derivatives of the longitudinal body profile, respectively—are plotted in Figure 17. The divergence parameter is η'/η, where $\eta = R(x)$ along the body and the prime notation denotes ordinary differentiation with respect to the axial coordinate x. The longitudinal curvature is denoted by κ, given as:

$$\kappa = \frac{-\eta''}{\left[1+(\eta')^2\right]^{3/2}} \tag{6}$$

where the negative is supplied to signify convex curvature as a positive value.

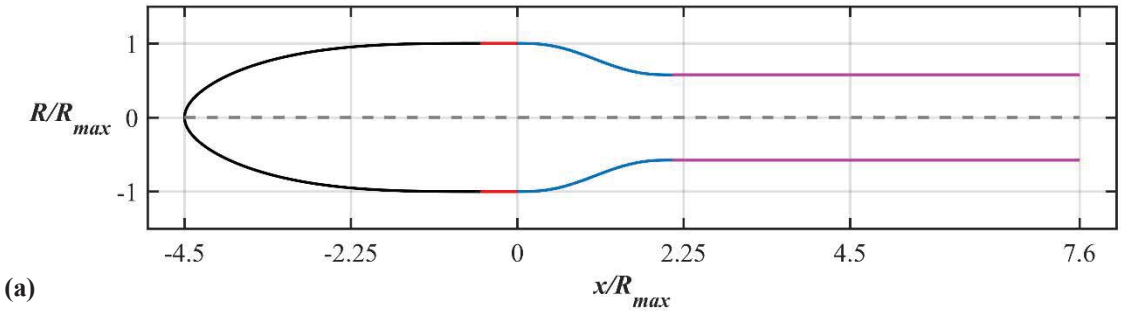

(a)

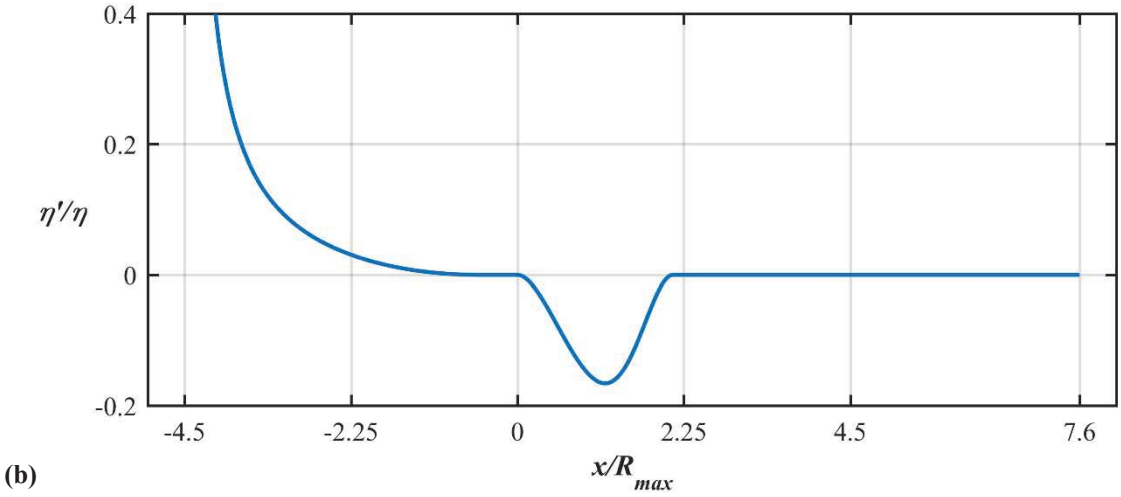

(b)

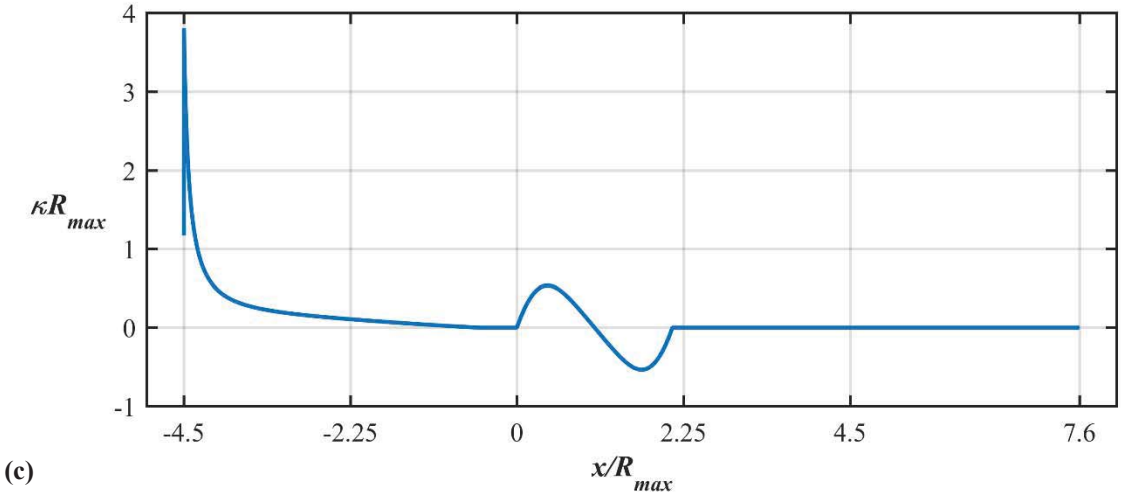

(c)

Figure 17. Geometry description for risk-reduction body.
Shown: (a) profile of revolution; (b) divergence parameter; (c) longitudinal curvature.
Note coordinate convention placing $x = 0$ at start of boattail section.

References

[1] Slotnick, J., Khodadoust, A., Alonso, J., Darmofal, D., Groff, W., Lurie, E., and Mavriplis, D., "CFD Vision 2030 Study: A Path to Revolutionary Computational Aerosciences," NASA CR-2014-218178, 2014.

[2] Rumsey, C.L., Neuhart, D.H., and Kegerise, M.A., "The NASA Juncture Flow Experiment: Goals, Progress, and Preliminary Testing (Invited)," *54th AIAA Aerospace Sciences Meeting,* AIAA Paper 2016-1557, 2016. doi: 10.2514/6.2016-1557.

[3] Oberkampf, W.L. and Roy, C.J., "Verification and Validation in Scientific Computing," Cambridge University Press, 2012.

[4] Watson, R.D., Anders, J.B., and Hall, R.M., "Skin Friction at very High Reynolds Numbers in the National Transonic Facility," NASA TP 2006-214497, 2006.

[5] Carlson, J.-R. and Reubush, D.E., "High Reynolds Number Analysis of an Axisymmetric Afterbody with Flow Separation," *19th AIAA Advanced Measurement and Ground Testing Technology Conference,* 1996. doi: 10.2514/6.1996-2274.

[6] Fluid Dynamics Panel Working Group 21, "A Selection of Test Cases for the Validation of Large-Eddy Simulations of Turbulent Flows," North Atlantic Treaty Organization Advisory Group for Aerospace Research & Development, AGARD-AR-345, Neuilly-sur-Seine, France, 1998.

[7] Winter, K.G., Rotta, J.C., and Smith, K.G., "Turbulent Boundary Layer Studies on a Waisted Body of Revolution in Subsonic and Supersonic Flow," Aeronautical Research Council R&M No. 3633, 1970.

[8] Bachalo, W.D. and Johnson, D.A., "Transonic, Turbulent Boundary-Layer Separation Generated on an Axisymmetric Flow Model," *AIAA Journal,* Vol. 24, No. 3, 1986, pp. 437-443. doi: 10.2514/3.9286.

[9] Driver, D.M., "Reynolds Shear Stress Measurements in a Separated Boundary Layer Flow," *22nd AIAA Fluid Dynamics, Plasma Dynamics, and Lasers Conference,* AIAA Paper 91-1787, 1991. doi: 10.2514/6.1991-1787.

[10] Alving, A.E. and Fernholz, H.H., "Mean-Velocity Scaling in and Around a Mild, Turbulent Separation Bubble," *Physics of Fluids,* Vol. 7, No. 8, 1995, pp. 1956-1969. doi: 10.1063/1.868772.

[11] Alving, A.E. and Fernholz, H.H., "Turbulence Measurements Around a Mild Separation Bubble and Downstream of Reattachment," *Journal of Fluid Mechanics,* Vol. 322, 1996, pp. 297-328. doi: 10.1017/S0022112096002807.

[12] Presz, W.M. and Pitkin, E.T., "Flow Separation Over Axisymmetric Afterbody Models," *Journal of Aircraft,* Vol. 11, No. 11, 1974, pp. 677-682. doi: 10.2514/3.60403.

[13] Reubush, D.E. and Putnam, L.E., "An Experimental and Analytical Investigation of the Effect on Isolated Boattail Drag of Varying Reynolds Number Up to $130x10^6$," NASA TN D-8210, 1976.

[14] Hammache, M., Browand, F.K., and Blackwelder, R.F., "Whole-Field Velocity Measurements Around an Axisymmetric Body with a Stratford-Smith Pressure Recovery," *Journal of Fluid Mechanics,* Vol. 461, 2002, pp. 1-24. doi: 10.1017/S0022112002008479.

[15] Smits, A.J. and Wood, D.H., "The Response of Turbulent Boundary Layers to Sudden Perturbations," *Annual Review of Fluid Mechanics,* Vol. 17, 1985, pp. 321-358. doi: 10.1146/annurev.fl.17.010185.001541.

[16] Parish, E.J. and Duraisamy, K., "A Paradigm for Data-Driven Predictive Modeling using Field Inversion and Machine Learning," *Journal of Computational Physics,* Vol. 305, 2016, pp. 758-774. doi: 10.1016/j.jcp.2015.11.012.

[17] Xiao, H., Wu, J.-L., Wang, J.-X., Sun, R., and Roy, C.J., "Quantifying and Reducing Model-Form Uncertainties in Reynolds Averaged Navier-Stokes Equations: A Data-Driven, Physics-Informed Bayesian Approach," *Journal of Computational Physics,* Vol. 324, 2016, pp. 115-136. doi: 10.1016/j.jcp.2016.07.038.

[18] Smits, A.J. and Joubert, P.N., "Turbulent Boundary Layers on Bodies of Revolution," *Journal of Ship Research,* Vol. 26, No. 2, 1982, pp. 135-147.

[19] Bradshaw, P., "Effects of Streamline Curvature on Turbulent Flow," North Atlantic Treaty Organization Advisory Group for Aerospace Research and Development, AGARD-ograph 169, Neuilly-sur-Seine, France, 1973.
[20] Robinson, R.C., Wilcox, P.R., Gambucci, B.J., and George, R.E., "Dynamic Response of a Family of Axisymmetric Hammerhead Models to Unsteady Aerodynamic Loading," NASA TN D-4504, 1968.
[21] Murman, S.M., Blonigan, P.J., and Diosady, L.T., "Comparison of Transonic Buffet Simulations with Unsteady PSP Measurements for a Hammerhead Payload Fairing," *55th AIAA Aerospace Sciences Meeting,* AIAA Paper 2017-1404, 2017. doi: 10.2514/6.2017-1404.
[22] Krist, S.L., Biedron, R.T., and Rumsey, C.L., "CFL3D User's Manual (Version 5.0)," NASA TM-1998-208444, 1998.
[23] Biedron, R.T., Carlson, J.-R., Derlaga, J.M., Gnoffo, P.A., Hammond, D.P., Jones, W.T., Kleb, B., Lee-Rausch, E.M., Nielsen, E.J., Park, M.A., Rumsey, C.L., Thomas, J.L., and Wood, W.A., "FUN3D Manual: 12.9," NASA TM-2016-219012, 2016.
[24] Ferrante, A. and Elghobashi, S.E., "A Robust Method for Generating Inflow Conditions for Direct Simulations of Spatially-Developing Turbulent Boundary Layers," *Journal of Computational Physics,* Vol. 198, No. 1, 2004, pp. 372-387. doi: 10.1016/j.jcp.2004.01.016.
[25] Tunnell, P.J., "An Investigation of Sting-Support Interference on Base Pressure and Forebody Chord Force at Mach Numbers from 0.60 to 1.30," NACA RM A54K16a, 1955.

REPORT DOCUMENTATION PAGE

Form Approved
OMB No. 0704-0188

1. REPORT DATE *(DD-MM-YYYY)*	2. REPORT TYPE	3. DATES COVERED *(From - To)*
01-11-2017	Technical Memorandum	January 2016 - July 2017

4. TITLE AND SUBTITLE

Development of an Axisymmetric Afterbody Test Case for Turbulent Flow Separation Validation

5a. CONTRACT NUMBER

5b. GRANT NUMBER

5c. PROGRAM ELEMENT NUMBER

6. AUTHOR(S)

Disotell, Kevin J.; Rumsey, Christopher L.

5d. PROJECT NUMBER

5e. TASK NUMBER

5f. WORK UNIT NUMBER

109492.02.07.01.01

7. PERFORMING ORGANIZATION NAME(S) AND ADDRESS(ES)

NASA Langley Research Center
Hampton, VA 23681-2199

8. PERFORMING ORGANIZATION REPORT NUMBER

9. SPONSORING/MONITORING AGENCY NAME(S) AND ADDRESS(ES)

National Aeronautics and Space Administration
Washington, DC 20546-0001

10. SPONSOR/MONITOR'S ACRONYM(S)

NASA

11. SPONSOR/MONITOR'S REPORT NUMBER(S)

NASA-TM-2017-219680

12. DISTRIBUTION/AVAILABILITY STATEMENT

Unclassified – Unlimited
Subject Category 34
Availability: NASA STI Program (757) 864-9658

13. SUPPLEMENTARY NOTES

An electronic version can be found at http://ntrs.nasa.gov

14. ABSTRACT

As identified in the CFD Vision 2030 Study commissioned by NASA, validation of advanced RANS models and scale-resolving methods for computing turbulent flows must be supported by improvements in high-quality experiments designed specifically for CFD implementation. A new test platform referred to as the Axisymmetric Afterbody allows for a range of flow behaviors to be studied on interchangeable afterbodies while facilitating access to higher Reynolds number facilities. A priori RANS computations are reported for a risk-reduction configuration to demonstrate critical variation among turbulence model results for a given afterbody, ranging from barely-attached to mild separated flow. The effects of body nose geometry and tunnel-wall boundary condition on the computed afterbody flow are explored to inform the design of an experimental test program.

15. SUBJECT TERMS

Aerodynamics; Computational Fluid Dynamics; Validation Experiments; Bodies of Revolution; Afterbodies; Turbulence Modeling; Wind Tunnels; Turbulent Boundary Layers; Flow Separation.

16. SECURITY CLASSIFICATION OF:			17. LIMITATION OF ABSTRACT	18. NUMBER OF PAGES	19a. NAME OF RESPONSIBLE PERSON
a. REPORT	b. ABSTRACT	c. THIS PAGE			STI Help Desk (help@sti.nasa.gov)
U	U	U	UU	34	19b. TELEPHONE NUMBER *(Include area code)* (757) 864-9658